Supplemental Material

Title:

Cerebral amyloid-β proteostasis is highly regulated by the membrane transport protein ABCC1 in mice

Authors:

Markus Krohn, Cathleen Lange, Jacqueline Hofrichter, Katja Scheffler, Jan Stenzel, Johannes Steffen, Toni Schumacher, Thomas Brüning, Anne-Sophie Plath, Franziska Alfen, Anke Schmidt, Felix Winter, Katja Rateitschak, Andreas Wree, Jörg Gsponer, Lary C. Walker & Jens Pahnke

Supplementary Information – include

Supplementary Methods/Equations

Mathematical modeling of Aβ kinetics

We developed a mathematical model to determine whether changes in monomeric Aβ excretion from the brain can lead to the different temporal aggregation profiles that we observed in mouse models. The main assumptions of the model and its structure are developed on the basis of our experimental data and on previously published results and hypotheses related to protein aggregation.
Owing to the multitude of mechanisms involved in the in vivo aggregation of Aβ, some of which almost certainly remain unknown, we did not attempt a detailed mechanistic mathematical representation. Instead we concentrated on distilling the available knowledge into a model that illuminates the underlying dynamics and provides explanations for the experimental observations in ABC transporter-deficient mice. The phenotypic changes in the different transgenic mice that we employed are the result of a complicated interplay between protein aggregation and aggregate removal processes. Nevertheless, our model reveals that these changes can be attributed to a few basic biological mechanisms.

To capture the main mechanisms underlying protein aggregation in Alzheimer's disease, we established a reduced biochemical reaction network that describes monomer secretion and Aβ aggregation. The underlying biochemical processes can be clustered into two interdependent modules:

i) *Module 1* describes the production of monomeric Aβ and its removal from the brain by cellular processes. Although the latter include processes such as enzymatic degradation and proteasomal degradation, our model focuses on active transport to capture the differences in the transgenic mouse strains.
ii) *Module 2* describes the aggregation of monomeric Aβ peptides that initially form nuclei and their subsequent growth by addition of monomers.

The two modules of our reaction network interact in two ways (see Figure 3):

i) *Module 1* and *Module 2* share the same pool of Aβ monomers, and
ii) insoluble aggregates of *Module 2* (the guanidine-soluble Aβ fraction) impede monomer removal described in *Module 1*.

By using these two modules, we can highlight the main mechanisms governing the temporal behavior of protein deposition in the brain: Aβ monomer abundance over time influenced by the production and removal by cellular machinery (*Module 1*) and the removal of Aβ monomers from the pool by aggregation (*Module 2*).

Assumptions for the biochemical network representing protein production, removal and aggregation

Assumptions for *Module 1*:

i) Our experimental data show constant APP expression by the transgene. We therefore assume constant monomer production in our transgenic model. This assumption has been used previously in Craft *et al*. (1).

ii) Monomeric Aβ can be removed by ABC transporters, see this paper and (2-4).

iii) Knockout of Aβ-excreting ABC transporters permanently decreases Aβ removal by active molecular transporters (this paper). Other mechanisms that clear Aβ from the brain, such as enzymatic cleavage and proteasomal degradation, are not affected by the ABC transporter knockouts (Supplementary Figure 4 and Supplementary Table 5).

iv) Removal of monomeric Aβ by ABC transporters is hampered by Aβ aggregates. Deposition of Aβ has been shown to be inversely correlated with ABCB1 expression in the elderly brain (3, 5). We assume that this negative correlation is the result of a causal relationship. As the immunohistochemical methods used by Vogelgesang *et al.* (3) only reveal insoluble Aβ aggregates; the negative causal relationship was restricted to insoluble Aβ.

Assumptions for *Module 2*:

i) The first step in Aβ aggregation is the formation of nuclei consisting of a fixed number of monomers. Nucleation is known to be an important first step in the aggregation of Aβ42, while the exact nucleus size is still a matter of discussion (6, 7).

ii) Aβ aggregation occurs by monomer addition to the nuclei. Sequential monomer addition is included in many models of protein aggregation; for a comparison see Bernacki *et al.* (8).

iii) Aggregation occurs at different rates. To reduce the reaction network's complexity, two groups of aggregates are considered according to our biological data: 'soluble' (i.e. buffer-soluble Aβ) and 'insoluble' (i.e. guanidine-soluble Aβ). We assume that all aggregates in one group are formed with the same aggregation constant.

iv) Breakage of Aβ aggregates is negligible for the reproduction of the experimentally measured temporal aggregation profile. Fibril breakage was considered during the construction of the mathematical model, but parameter value estimation suggested that fibril breakage has no influence.

Translation of the biochemical reaction network into a mathematical model

The network was translated into a system of algebraic and ordinary differential equations that describe the temporal changes of aggregate concentrations as a function of the aggregation and transport processes.

Implementation of assumptions in *Module 1*:

i) Constant monomer production:
Production of monomeric Aβ is modeled by a constant production term p.

ii) Removal of monomeric Aβ by ABC transporters:

In order to reduce the complexity of the model, all transport mechanisms are merged into one term. We define the transport rate R_T as the product of a constant parameter c_T, which we call the *clearance capacity*, and the available monomers *M*. $R_T = c_T \cdot M$

iii) Knockouts of Aβ-excreting ABC transporters permanently decrease Aβ removal by active molecular transporters.
This assumption is not expressed in the equations of the model. Instead it is used to predict the influence of ABC transporter deficiency in the mouse models.

iv) Larger aggregates impede removal of monomeric Aβ:
To mathematically realize this assumption, we calculate the net inflow I_{net} into the pool of monomeric Aβ as the difference of its constant production *p* and the removal of monomeric Aβ by the ABC transporters. The transport is characterized by its activity a_T, being the product of the transport rate, R_T, and a term describing the impeding influence of the insoluble aggregates. This leads to the following equation for the net inflow:

$$I_{net} = p - a_T, \quad I_{net} \overset{!}{\geq} 0.$$

Parameters are constrained such that I_{net}, p and R_T are positive. According to the information above, a_T is given by

$$a_T = R_T \cdot \frac{s_T{}^{e_T}}{s_T{}^{e_T} + L^{e_T}},$$

The term $\frac{s_T{}^{e_T}}{s_T{}^{e_T} + L^{e_T}}$ describes the negative influence of insoluble aggregates (*L*) on transporter activity. s_T and e_T are two shape parameters that allow the description of vast possibilities of different interactions. Modeling the negative influence of insoluble Aβ on the transport mechanism in the given way guarantees that

i) the activity a_T of the transport mechanism is always larger than zero and smaller than the transport rate R_T,

ii) a_T decreases with increasing values of *L*,

iii) we provide a general and simple description of a broad range of possible mechanisms leading to the reduction of monomeric Aβ transport.

Implementation of assumptions in *Module 2*:

i) The first step in Aβ aggregation is the formation of nuclei consisting of n_n monomers. The reaction rate for the production of nuclei depends on the nucleation constant k_n and the monomer concentration *M*.
Accordingly, the rate for monomer decrease is: $-k_n \cdot n_n \cdot M^{n_n}$ while the quantity of nuclei is increased at rate $k_n \cdot M^{n_n}$.

ii) Aβ aggregation occurs by subsequent monomer addition to the nuclei:
Each aggregate A_j of size *j* is formed by addition of one monomer to one aggregate of size *j-1*.

Two groups of aggregates are being considered according to the buffer solubility: ‘soluble’ and ‘insoluble’. Two different reaction constants are used to describe the differences in the formation of the two groups of aggregates.

The soluble pool of aggregates consists of the monomers, the nuclei and all aggregates up to the size n_s. The insoluble pool of aggregates contains all aggregates from size (n_s+1) up to the largest modeled aggregate of size n_i. Hence, n_n (nucleus size), n_s (number of monomers in the largest aggregate in soluble pool), and n_i (number of monomers in the largest aggregate considered in the model) are the only three integer-valued parameters in the model. Their respective values are discussed in the section on parameter estimation and are listed in Supplementary Table 1.

Rate constants for aggregation are assigned to both the pool of soluble and the pool of insoluble Aβ. These are named k_{sol} and k_{insol}, respectively. Depending on the pool an aggregate belongs to, the aggregation rate is computed as $k_{sol} \cdot A_j \cdot M$ or $k_{insol} \cdot A_j \cdot M$. The A_j denotes the concentration of aggregates of size j.

Equations of the model

The net inflow I_{net} (i.e. export-reduced production of Aβ) of monomers to the system is calculated by the following equation:

$I_{net} = p - a_T, \quad I_{net} \overset{!}{\geq} 0$	Net inflow is equal to the production minus the remaining activity of the transport mechanism.

According to the formulation of the term describing the impeding influence of the insoluble pool of aggregates, the activity of the transport mechanism decreases if the concentration of insoluble Aβ increases.

The temporal changes in the concentration of monomers, nuclei (N) and all other aggregates (A_{n_n+1} to A_{n_i}) are described by the following equations, where subscripts on the aggregates A indicate the number of monomers comprising them.

$\frac{dM}{dt} = I_{net} - k_n \cdot n_n \cdot M^{n_n}$	Net inflow and free monomer decrease by nucleation.
$- k_{sol} \cdot N \cdot M$	Free monomer decrease by monomer addition to a nucleus.
$- k_{sol} \cdot A_{n_n+1} \cdot M$	Free monomer decrease by monomer addition to an aggregate of size n_n+1.
$- k_{sol} \cdot A_{n_n+2} \cdot M$	Free monomer decrease by monomer addition to an aggregate of size n_n+2.
$\vdots$	

$-k_{sol} \cdot A_{n_s-1} \cdot M$ $-k_{insol} \cdot A_{n_s} \cdot M$ $\vdots$ $-k_{insol} \cdot A_{n_i-1} \cdot M$	Free monomer decrease by monomer addition to an aggregate of size $n_{s\text{-}1}$. Free monomer decrease by monomer addition to an aggregate of size n_s. Free monomer decrease by monomer addition to an aggregate of size $n_{i\text{-}1}$.
$\frac{dN}{dt} = k_n \cdot M^{n_n} - k_{sol} \cdot N \cdot M$	Nuclei produced by monomer nucleation minus nuclei converted to larger aggregates by monomer addition.
$\frac{dA_{n_n+1}}{dt} = k_{sol} \cdot N \cdot M - k_{sol} \cdot A_{n_n+1} \cdot M$	Aggregates of size n_n+1 produced by monomer addition to nuclei minus aggregates converted to larger aggregates by monomer addition.
$\frac{dA_j}{dt} = k_{sol} \cdot A_{j-1} \cdot M - k_{sol} \cdot A_j \cdot M,$ $j = (n_n + 2, \ldots, n_s - 1)$	Aggregates of size j produced by monomer addition to aggregates of size (j-1) minus aggregates of size j converted to larger aggregates by monomer addition.
$\frac{dA_{n_s}}{dt} = k_{sol} \cdot A_{n_s-1} \cdot M - k_{insol} \cdot A_{n_s} \cdot M$	Aggregates of size n_s produced by monomer addition to aggregates of size (n_s-1) minus aggregates converted to larger aggregates by monomer addition.
$\frac{dA_j}{dt} = k_{insol} \cdot A_{j-1} \cdot M - k_{insol} \cdot A_j \cdot M,$ $j = n_s + 1, \ldots, n_i - 1$	Aggregates of size j produced by monomer addition to aggregates of size (j-1) minus aggregates of size j converted to larger aggregates by monomer addition.
$\frac{dA_{n_i}}{dt} = k_{insol} \cdot A_{n_i-1} \cdot M$	Aggregates of size n_i produced by monomer addition to aggregates of size (n_i-1).

The model was implemented in Matlab 7.10 (The Mathworks, Inc. Natick, Massachusetts).

Estimation of parameter values

Our model has ten unknown parameters, three of them integer-valued and seven real-valued. To compare the model simulations with experimental data, we fixed the three integer-valued parameters using the values presented in Supplementary Table 1. This allows for the estimation of real-valued parameters from experimental time series using nonlinear global optimization. n_n was set to 6, according to the hexamer paranucleus considered by Bernstein *et al.* (7) . Being aware of the ongoing discussion about the "true" nucleus size, we also tested our model with n_n = 5 as suggested by Ahmed *et al.* (6), with comparable results (not shown here.) Because our objective is a phenomenological model rather than a mechanistic one, there is no way to assess this parameter to be "right" or "wrong". The same argument holds for the other two integer parameters, n_s (number of monomers in the largest aggregate in

soluble pool), and n_i (number of monomers in the largest aggregate considered in the model), which are not to be interpreted in a mechanistic sense.
The variables of the mathematical model are given in units of aggregate numbers normalized to total protein mass. The ELISA measurements are given in *ng/mg* where *ng* refers to mass of Aβ and *mg* refers to the total protein mass of the soluble and insoluble fraction, respectively. To compare model simulations with experimental data we transformed the variables of the model to new variables such that the new variables have the unit *ng/mg*. This was done by the following steps: The mass of an Aβ monomer is X = 4 kDa which can be transformed to $X = 6.642 \cdot 10^{-12}$ ng. We multiplied each equation by X. Then we introduced new variables $M´,N´,A_j´$ and new parameters which are defined as follows:

$M' = X \cdot M$	Concentration of monomers in ng/mg
$N' = X \cdot N$	Concentration of nuclei in ng/mg
$A_j' = X \cdot A_j,\ j = n_{n+1}, \ldots, n_i$	Concentration of different aggregates in ng/mg
$k_n' = k_n \cdot X^{-n_n+1}$	Nucleation constant
$k_{sol}' = k_{sol} \cdot X^{-1}$	Aggregation constant for soluble aggregates
$k_{insol}' = k_{insol} \cdot X^{-1}$	Aggregation constant for insoluble aggregates
$p' = X \cdot p$	Production rate of monomeric beta-Amyloid
$s_T' = X \cdot s_T$	Shift parameter for transport mechanism

The physical interpretation of the new variables is the still the same as for the old variables: each variable value is proportional to the number of the respective aggregate though the new variables have the unit *ng/mg*. Then the concentration of monomeric Aβ included in each aggregate was calculated by multiplying the concentration of the aggregate described by the new variables with the number of monomers. In a second step, the concentration of monomers in the pool of soluble Aβ and the concentration of monomers in the pool of insoluble Aβ were computed as the sum of monomer concentrations in all aggregates belonging to the respective pools.
To evaluate the ability of our model to reproduce the experimentally obtained ELISA measurements from APP/PS1xABCC1$^{-/-}$ mice, we determined the values of the real-valued parameters and the initial monomer concentration by global optimization. We chose only the soluble Aβ ELISA measurements for optimization. This was done because soluble Aβ is thought to contain the most toxic aggregates, and is therefore the main subject of interest (9). Furthermore, the accumulation of insoluble Aβ is a passive process that depends directly on the concentration of soluble Aβ. The squared difference between the simulation results for soluble Aβ monomers and the ELISA measurements of soluble Aβ in APP/PS1xABCC1$^{-/-}$ mice was minimized by global optimization using the PSwarmM Software v1.4 (10). The results of parameter optimization are presented in Supplementary Tables 2 and 3.

Model simulations and model validation
The numerical solution of the ordinary differential equations with optimized parameters led to temporal concentration profiles for soluble Aβ (buffer-soluble) and for insoluble Aβ

(guanidine-soluble), shown in Figure 4A-B in the main text. The simulations of the mathematical model with optimized parameters closely matched the characteristics of in vivo Aβ accumulation in APP/PS1x ABCC1$^{-/-}$ mice. Although the values for the seven real-valued parameters were estimated to represent the soluble Aβ42 concentrations measured by ELISA only, the resulting simulation predicted the temporal aggregation profile for insoluble Aβ42 concentrations surprisingly well. This suggests that our model captures the main mechanisms underlying the aggregation of Aβ42 in APP/PS1xABCC1$^{-/-}$ mice.

To validate our assumption that a change in monomeric Aβ could result in different temporal aggregation profiles observed in the mouse models with different transporter knockouts, we investigated the model's behavior using the initial parameter set with only one parameter being changed. Assuming that the knockout of the ABC transporters permanently decreases Aβ removal from the brain, we fixed all parameters except the clearance capacity c_T. Increasing the clearance capacity by only 11% (as compared to APP/PS1xABCC1$^{-/-}$ mice) lead to the slower aggregation profile observed in APP/PS1xABCB1$^{-/-}$ mice (Figure 4C-D in the main text).

Interestingly, our results are obtained without consideration of fibril breakage. As fibril breakage has been discussed as a factor in the seeding of Aβ deposition (11), we initially included the possibility of fibril breakage in our model. Parameter value estimation resulted in a value of zero for the breakage constant.

Supplementary Figures

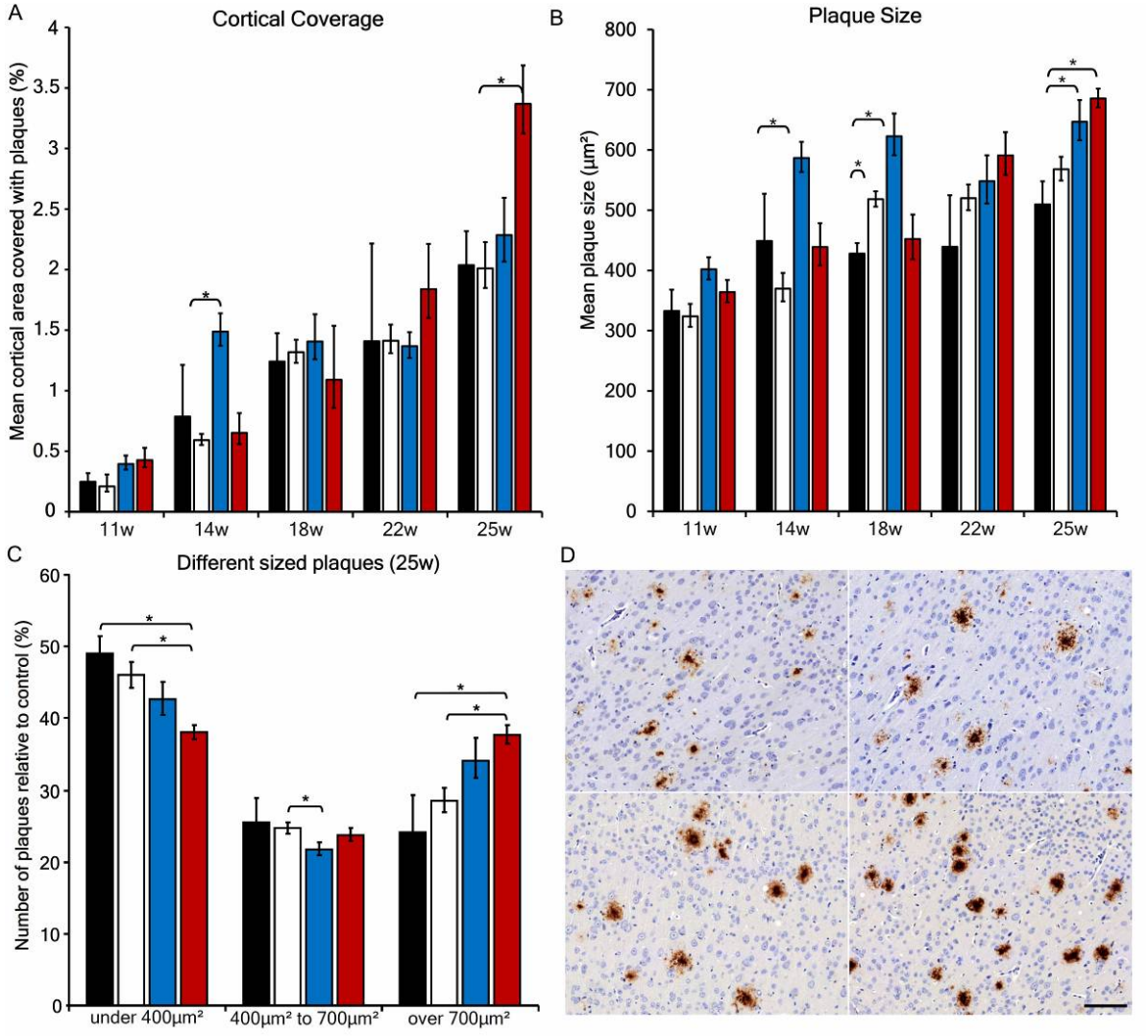

Supplementary Figure 1. Quantification of Aβ deposition using immunohistochemistry

(**A**) Cortical areal density (coverage) and size of plaques are increased in specific ABC transporter knockout mice (controls ■, APP/PS1xABCG2$^{-/-}$ □, APP/PS1xABCB1$^{-/-}$ ■, APP/PS1xABCC1$^{-/-}$ ■). APP/PS1xABCC1$^{-/-}$ mice show the greatest β-amyloid burden. (n≥5)
(**B**) Overall plaque size is increased in APP/PS1xABCC1$^{-/-}$ and APP/PS1xABCB1$^{-/-}$ mice at the age of 25 weeks. (n≥5)
(**C**) The overall increase in plaque size is associated with the occurrence of fewer small plaques and more large plaques (>700 µm^2), whereas the numbers of medium-sized plaques remain at the same levels in 25 week-old animals. (n≥5)
(**D**) Cortical plaque size and staining intensity are elevated in APP/PS1xABCC1$^{-/-}$ mice (top left - APP/PS1; top right - APP/PS1xABCG2$^{-/-}$; bottom left - APP/PS1xABCB1$^{-/-}$; bottom right - APP/PS1xABCC1$^{-/-}$). Anti-Aβ (6F3D) staining. Scale bar = 100 µm, age 25 weeks.

Error bars = s.e.m.,* $p<0.05$

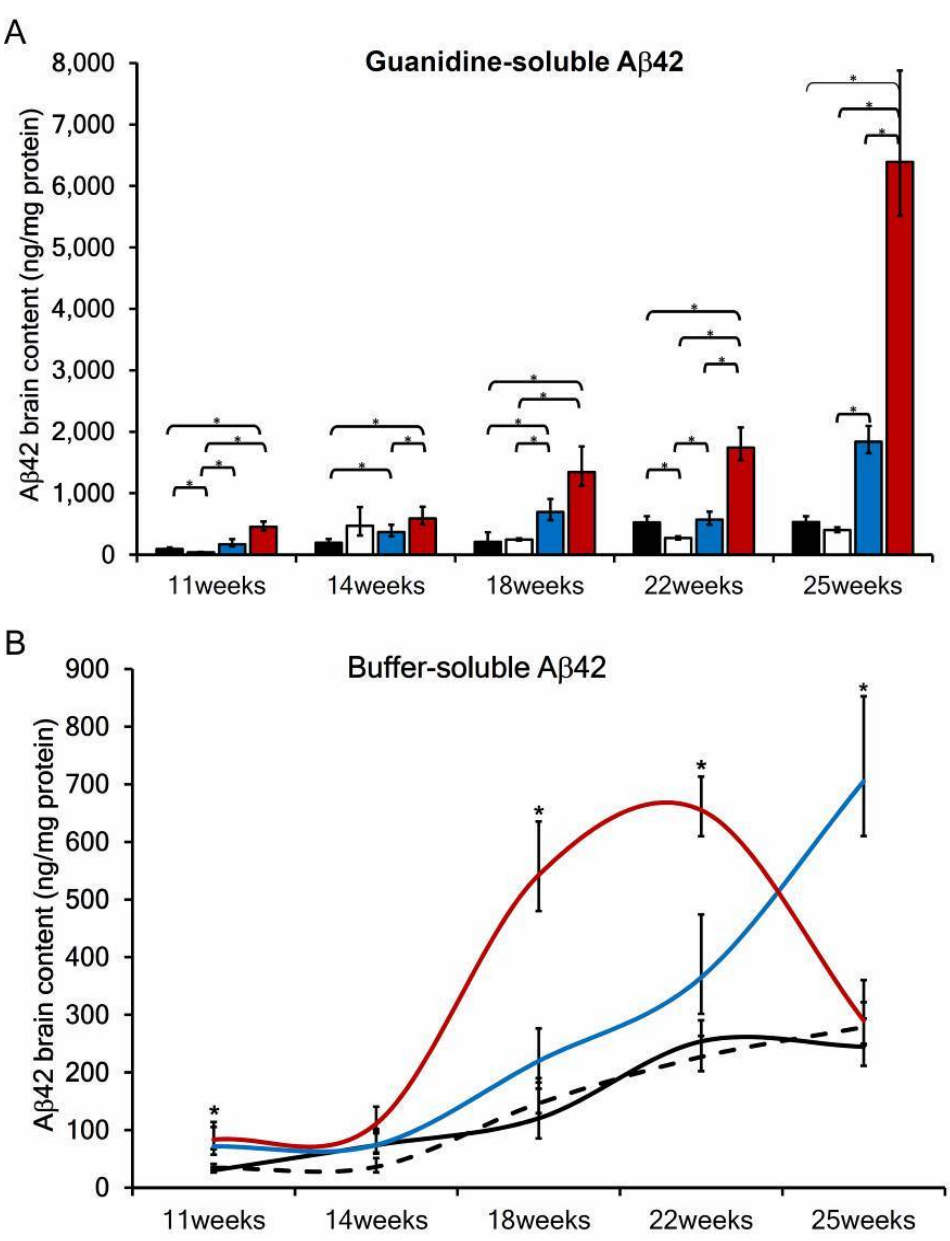

Supplementary Figure 2. Age-related Aβ42 concentrations measured by ELISA

(**A**) A strong increase in guanidine-soluble Aβ42 content was observed in APP/PS1xABCC1$^{-/-}$ mice ■ (up to 12-fold in APP/PS1xABCC1$^{-/-}$ mice and 3.5-fold in APP/PS1xABCB1$^{-/-}$ mice ■ vs. controls ■). APP/PS1xABC1$^{-/-}$ and APP/PS1xABCB1$^{-/-}$ mice showed increased Aβ42 levels even at early time points in the analyzed time series. APP/PS1xABCG2$^{-/-}$ mice □ showed no differences as compared to controls. (n≥4)

(**B**) Buffer-soluble Aβ42 increases rapidly between 14w and 18w of age in APP/PS1xABCC1$^{-/-}$ mice ■. A similar increase is found in APP/PS1xABCB1$^{-/-}$ mice ■ with a delay of approximately 6 weeks. After 22 weeks, there is a sharp decline in soluble Aβ42 in APP/PS1xABCC1$^{-/-}$ mice, possibly owing to sequestration of the peptide in cerebral Aβ deposits. Controls ■ , APP/PS1xABCG2$^{-/-}$ mice dotted line. (n≥4)

Error bars = s.e.m., * $p<0.05$

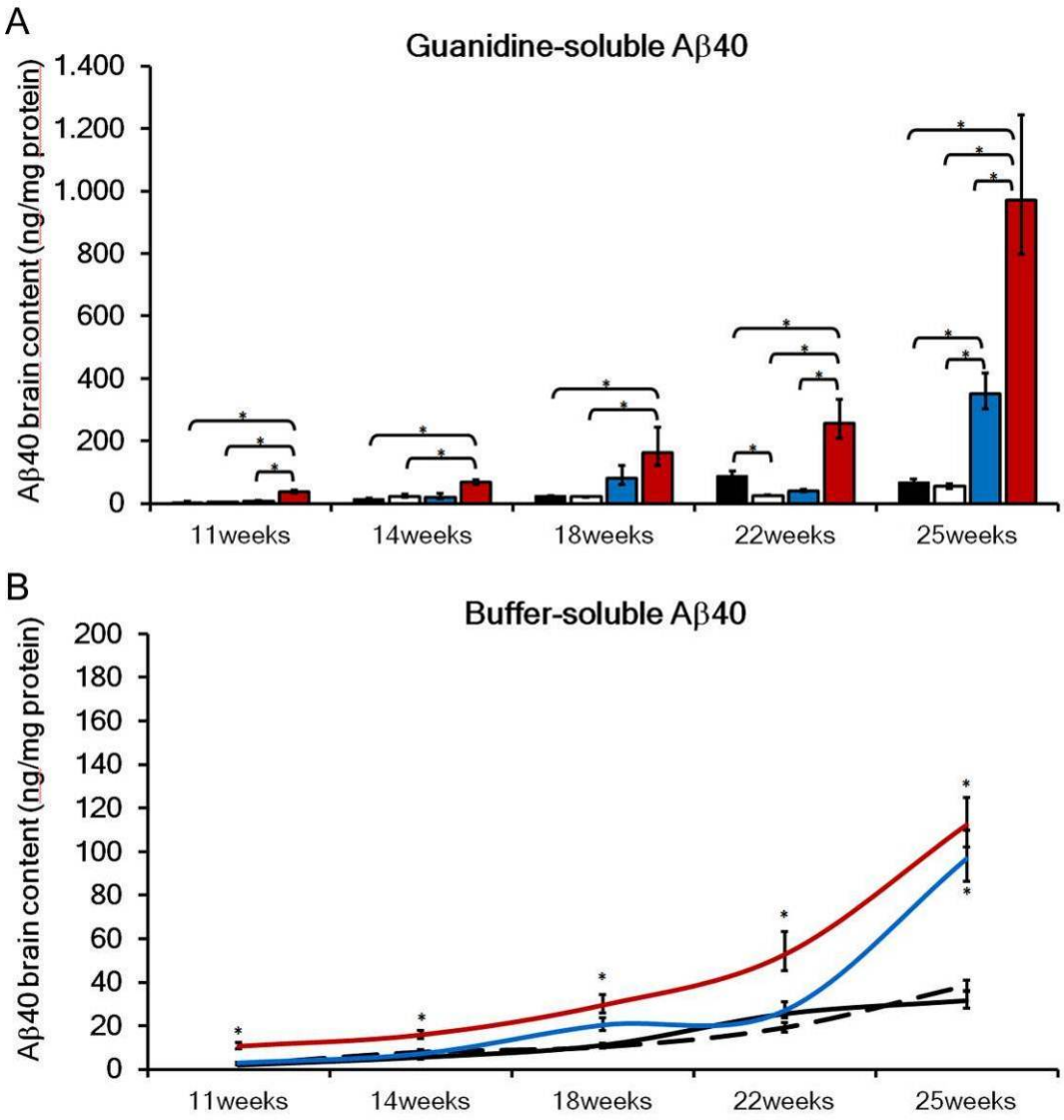

Supplementary Figure 3. Age-related Aβ40 concentrations measured by ELISA

(**A**) A strong increase in guanidine-soluble Aβ40 content was observed in APP/PS1xABCC1$^{-/-}$ mice ■ (up to 14-fold in APP/PS1xABCC1$^{-/-}$ mice and 5-fold in APP/PS1xABCB1$^{-/-}$ mice ■ vs. controls ■). APP/PS1xABC1$^{-/-}$ and APP/PS1xABCB1$^{-/-}$ mice showed increased Aβ40 levels even at early time points in the analyzed time series. APP/PS1xABCG2$^{-/-}$ mice □ showed no differences as compared to controls. Guanidine-soluble Aβ40 accumulation parallels that of Aβ42. (n≥4)

(**B**) Buffer-soluble Aβ40 increases rapidly between 18w and 25w of age in APP/PS1xABCC1$^{-/-}$ mice ■. Possibly due to its lower aggregation propensity, buffer-soluble Aβ40 levels do not decline precipitously like Aβ42 from age 22 weeks to 25weeks. Controls ■ , APP/PS1xABCB1$^{-/-}$ ■APP/PS1xABCG2$^{-/-}$ mice dotted line. (n=4)

Error bars = s.e.m., * $p<0.05$

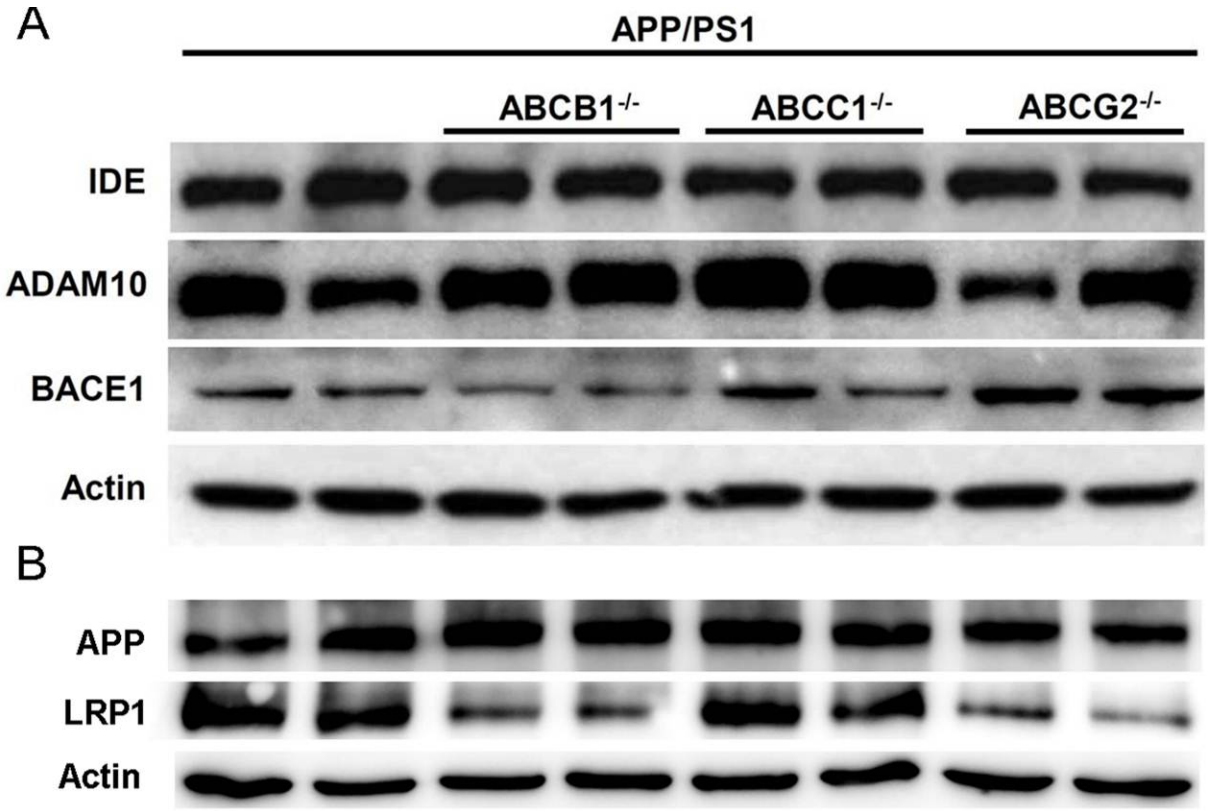

Supplementary Figure 4. Differences in APP processing do not account for accelerated Aβ accumulation in APP/PS1xABCB1$^{-/-}$ and APP/PS1xABCC1$^{-/-}$ mice

(**A**) Immunoblotting revealed a compensatory increase of ADAM10 in APP/PS1xABCB1$^{-/-}$ and APP/PS1xABCC1$^{-/-}$ mice that corresponds to the higher Aβ load. β-secretase (BACE1) expression was increased in APP/PS1xABCG2$^{-/-}$ mice only. Insulin-degrading enzyme (IDE) expression was not significantly altered. (**B**) APP transgene expression was unchanged in all strains. LRP1 abundance was significantly lower in APP/PS1xABCB1$^{-/-}$ and APP/PS1xABCG2$^{-/-}$ mice, whereas APP/PS1xABCC1$^{-/-}$ mice exhibited similar levels to APP/PS1 controls. (n=5, 10µg each, pooled)

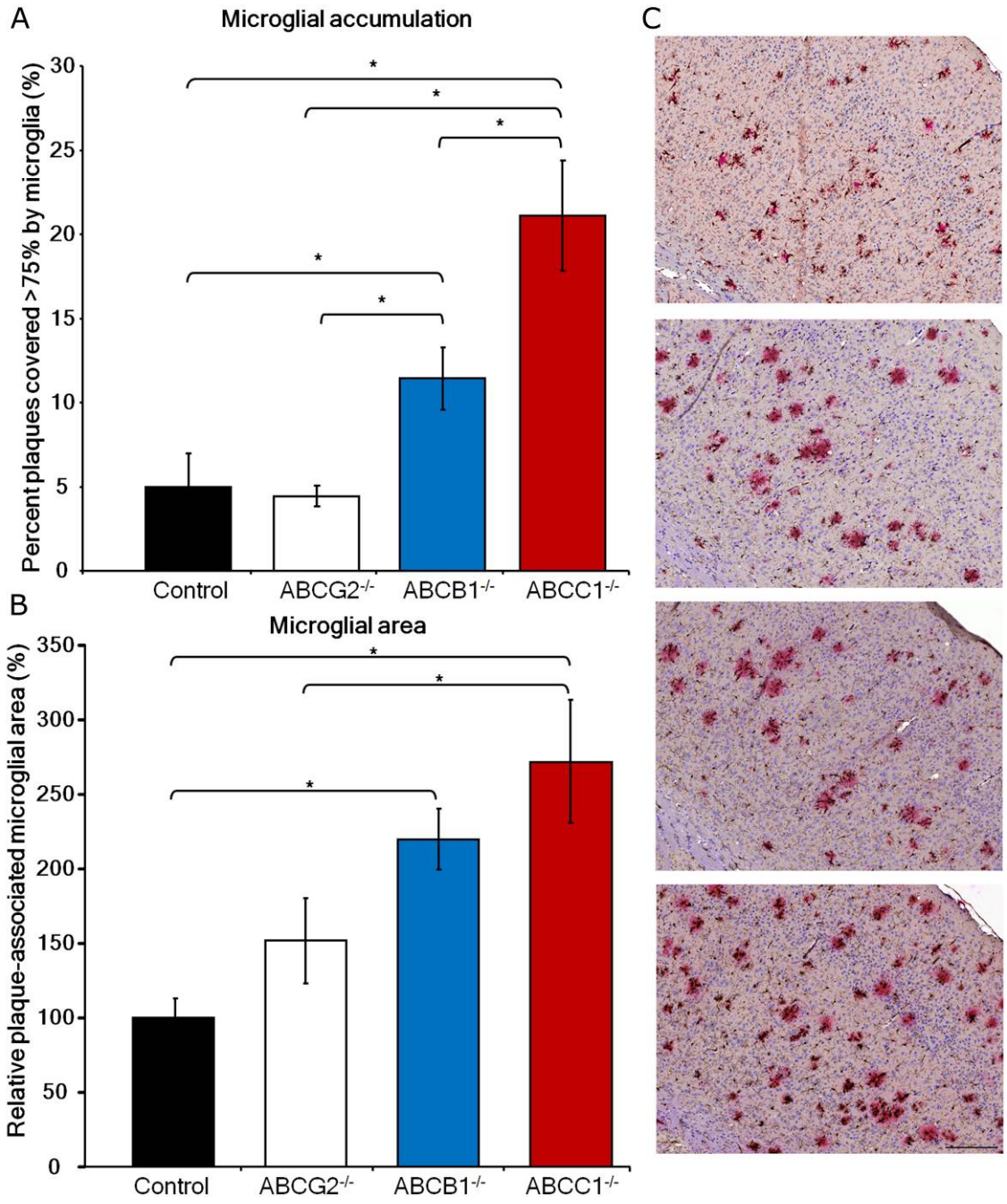

Supplementary Figure 5. Microglial density increases with increasing Aβ content but is not associated with reduced Aβ load in APP/PS1xABCC1$^{-/-}$ mice

(**A**) Area covered by microglia associated with Aβ deposits in the neocortex.
(**B**) The percentage of Aβ plaques that are densely covered (≥75%) by microglia is increased in both APP/PS1xABCC1$^{-/-}$ and APP/PS1xABCB1$^{-/-}$ mice, but not in APP/PS1xABCG2$^{-/-}$ mice. (n≥5) Error bars = s.e.m., * $p<0.05$
(C) Representative images of Iba1-Aβ double IHC staining in comparable regions of the frontal neocortex. Microglia (anti-Iba1) are shown in brown and Aβ (anti-Aβ(6F3D)) in red. From top to bottom, the photos show APP/PS1, APP/PS1xABCG2$^{-/-}$, APP/PS1xABCB1$^{-/-}$, and APP/PS1xABCC1$^{-/-}$ mice. Scale bar = 100μm

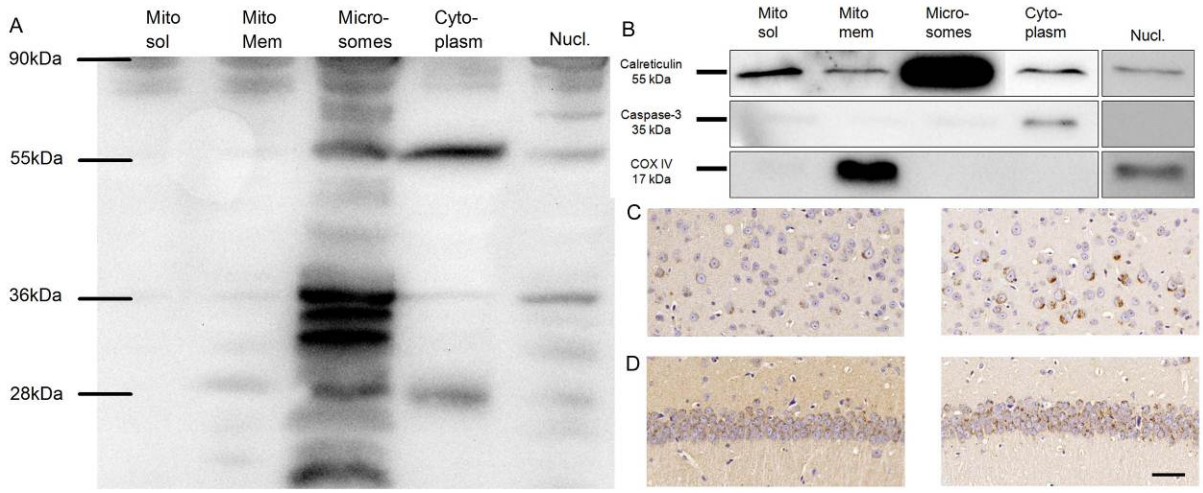

Supplementary Figure 6. Localization of intracellular $A\beta_{dt}$

(**A**) Western blot of subcellular fractions of brain tissue from $APP_{dt}/ABCC1^{-/-}$ mice (anti-Aβ, clone 6E10) reveals a predominant microsomal localization of antigen.
(**B**) Marker proteins of fractions show minor microsomal contamination of the other fractions.
(**C-D**) Immunohistochemical staining for Aβ (anti-Aβ42) reveals heavy intraneuronal accumulation of $A\beta_{dt}$ at age 16 months, especially in neocortical layer 5 (**C**) and hippocampal CA-regions (**D**); the left column shows a control mouse, the right column shows an $APP_{dt}/ABCC1^{-/-}$ mouse. Pyramidal neurons have been found to express ABCB1 and ABCC1, providing a potential link to the augmented intracellular accumulation of Aβ (12). Scale bar = 50 µm.

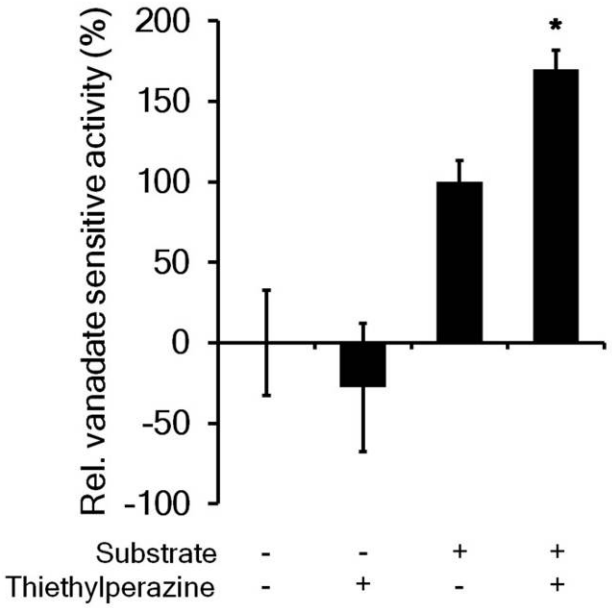

Supplementary Figure 7. Thiethylperazine enhances ABCC1 transport activity

ABCC1 activity assay using NEM-GS as substrate supports the data of Wesolowska et al. (13). Thiethylperazine enhanced ABCC1 activity for the assay substrate. Furthermore, the data revealed that thiethylperazine is an activator but not a substrate, since no activation is measured in the absence of NEM-GS.

Error bars, s.e.m., (n=3, *$p<0.05$).

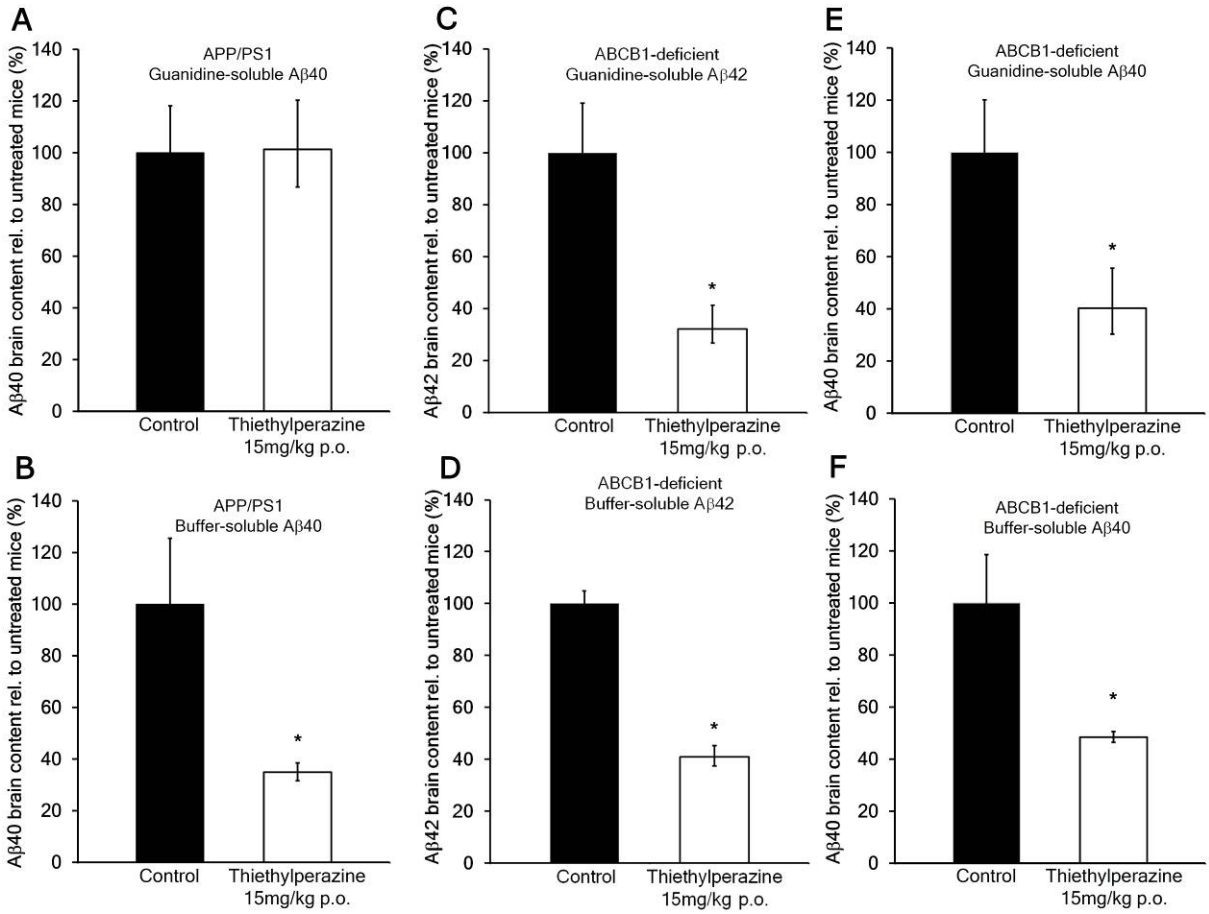

Supplementary Figure 8. A therapeutic treatment paradigm (day 75 - day 100) with thiethylperazine reduces Aβ40 levels

Mice treated p.o. with 15mg/kg/day thiethylperazine (ABCC1 activator and ABCB1 inhibitor (13)). (**A-B**) Only buffer-soluble Aβ40 is reduced in APP/PS1 mice, whereas (**C-F**) buffer-soluble and guanidine-soluble Aβ40 and Aβ42 are even more reduced in ABCB1-deficient mice as compared to the p.o. treatment of APP/PS1 mice (Figure 6 in the main text) supporting ABCC1 as primary target for Aβ reduction.

Error bars, s.e.m., ($n \geq 4$, $^*p < 0.05$).

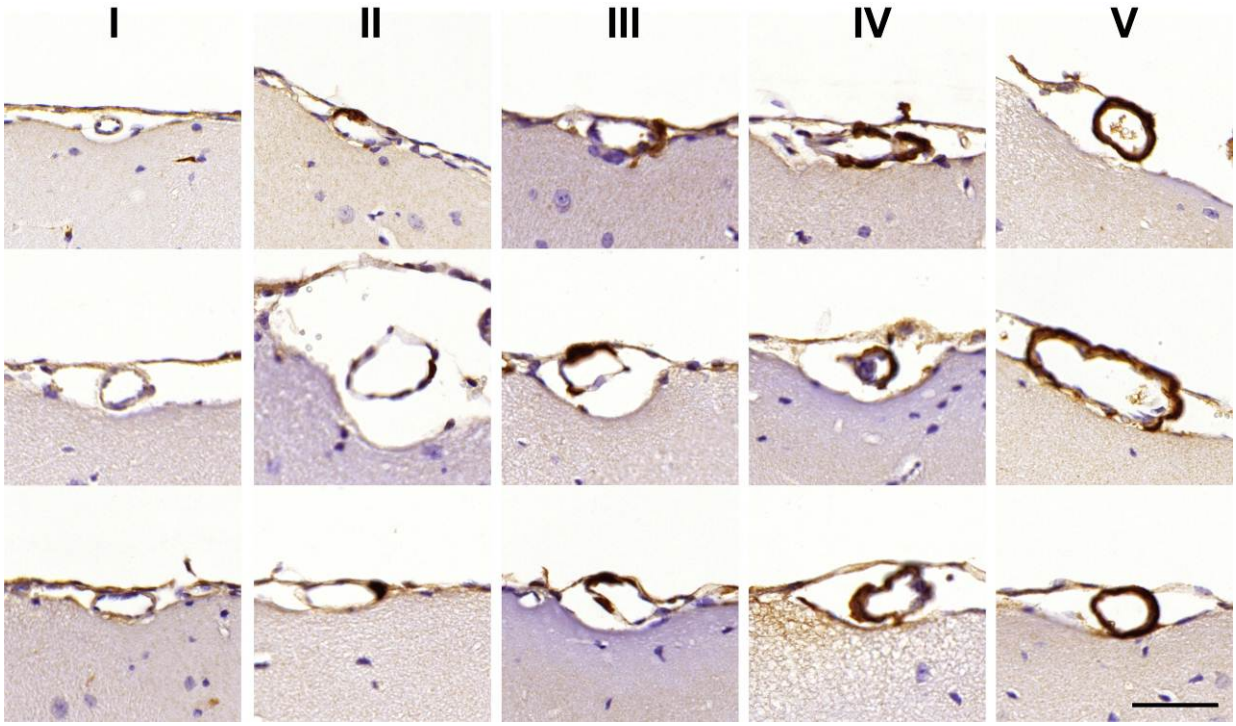

Supplementary Figure 9. Categorization of cerebral amyloid angiopathy severity in APP_{dt} – transgenic mice

I - no Aβ positivity at the vessel wall; II ≤25% of the circumference labeled; III 26-50% of the circumference labeled; IV 51-75% of the circumference labeled; and V >75% of the circumference labeled.

Supplementary Tables

Parameter	Value	Explanation
n_n	6	Number of monomers in the nucleus
n_s	15	Number of monomers included in the largest aggregate belonging to the soluble pool
n_i	55	Number of monomers in the largest aggregate belonging to the insoluble pool

Supplementary Table 1. Integer parameters used in the model

Parameter	Value	Explanation
p'	$91.239\ t^{-1} \cdot \left[\frac{X}{mg}\right]$	Production rate of monomeric Aβ
k_n'	$0.345\ t^{-1} \cdot \left[\frac{X}{mg}\right]^{-n_n+1}$	Nucleation constant
k_{sol}'	$0.342\ t^{-1} \cdot \left[\frac{X}{mg}\right]^{-1}$	Aggregation constant for soluble aggregates
k_{insol}'	$0.358\ t^{-1} \cdot \left[\frac{X}{mg}\right]^{-1}$	Aggregation constant for insoluble aggregates
s_T'	$17.744\left[\frac{X}{mg}\right]$	Shift parameter for transport mechanism
e_T	7.811	Exponent for transport mechanism (dimensionless)
c_T	$82.419\ t^{-1}$	Capacity of the transport mechanism

Supplementary Table 2. Real-valued parameters for the mathematical model with variables in units *ng/mg*. The time scale for the model simulation was 50 to 200 days. $X = 6.642 \cdot 10^{-12}$ ng (4 kDa) is the mass of an Aβ monomer.

Species	Initial concentration	Explanation
$M'(t_0)$	$1.0439\ \frac{X}{mg}$	Initial monomer concentration

Supplementary Table 3. Initial concentration of monomers (t_0 = 50 days) used for the simulation of the mathematical model with variables in units *ng/mg*. The initial concentration for all other species was set at zero. $X = 6.642 \cdot 10^{-12}$ ng is the mass of an Aβ monomer.

	11w	14w	18w	22w	25w
ABCC1$^{-/-}$					
P-value*	0.714	0.304	0.252	0.194	0.061
P-value**	0.324	0.023	0.916	0.749	0.159
n	7	9	8	10	9
skewness	-0.48	-0.24	0.61	0.79	0.27
ABCC1$^{-/-}$					
P-value*	0.804	0.022	0.756	0.971	0.004
P-value**	0.834	0.348	0.297	0.483	0.015
n	6	8	8	10	9
skewness	0.16	1.20	0.13	-0.18	1.68
control					
P-value*	0.162	0.612	0.127	0.082	0.546
P-value**	0.826	0.254	0.036	0.355	0.834
n	9	8	4	7	6
skewness	1.35	-0.60	-0.70	1.11	0.14
control					
P-value*	0.487	0.227	0.794	0.305	0.219
P-value**	0.978	0.544	0.901	0.188	0.239
n	9	9	4	7	6
skewness	0.68316	0.21302	0.4529	-0.51367	0.48191
ABCG2$^{-/-}$					
P-value*	0.545	***	0.830	0.615	0.977
P-value**	0.982		0.840	0.607	0.865
n	11		9	9	6
skewness	0.6402		0.17733	0.079067	0.20947
ABCG2$^{-/-}$					
P-value*	0.143		0.448	0.234	0.082
P-value**	0.355		0.845	0.032	0.019
n	11		9	9	6
skewness	1.00		0.75292	-0.35254	-0.16778
ABCB1$^{-/-}$					
P-value*	0.322	0.500		0.056	0.209
P-value**	0.483	0.862		0.436	0.560
n	7	5		7	9
skewness	0.27659	0.61884		0.75338	0.80
ABCB1$^{-/-}$					
P-value*	0.023	0.349		0.007	0.428
P-value**	0.457	0.885		0.054	0.292
n	8	5		7	8
skewness	0.52834	0.69379		1.4496	-0.24686

* for assumption of normally distributed data

** assumption of log normally distributed data

*** data for grey fields are omitted for statistics due to small sample size (n<4)

Supplementary Table 4. Statistics of ELISA samples

Gene assignment	Gene Symbol	p-value ($<10^{-4}$ significant)	Fold-Change	SS (Attri-bute)	SS (Error)
NM_007425 // Ager // advanced glycosylation end product-specific receptor	Ager/ RAGE	0.6772	**-1.0126**	0.1454	0.0126
NM_008512 // Lrp1 // low density lipoprotein receptor-related protein 1	Lrp1	0.4267	**-1.0509**	0.0693	0.0514
NM_011792 // Bace1 // beta-site APP cleaving enzyme 1	Bace1	0.9784	**-1.0014**	0.0003	0.0372
NM_019517 // Bace2 // beta-site APP-cleaving enzyme 2	Bace2	0.1807	**1.1336**	0.1369	0.1015
NM_019517 // Bace2 // beta-site APP-cleaving enzyme 2	Bace2	0.5732	**-1.0508**	0.0287	0.1057
NM_146104 // Aph1a // anterior pharynx defective 1a homolog (C. elegans)	Aph1a	0.2666	**1.0290**	0.0037	0.0082
NM_146104 // Aph1a // anterior pharynx defective 1a homolog (C. elegans)	Aph1a	0.6112	**1.0152**	0.0055	0.0121
NM_177583 // Aph1b // anterior pharynx defective 1b homolog (C. elegans)	Aph1b	0.0189	**-1.1419**	0.1473	0.0235
NM_026674 // Aph1c // anterior pharynx defective 1c homolog (C. elegans)	Aph1c	0.2457	**-1.0634**	0.0695	0.0341
NM_008943 // Psen1 // presenilin 1	Psen1	0.0936	**1.0529**	0.0095	0.0097
NM_011183 // Psen2 // presenilin 2	Psen2	0.4747	**1.0279**	0.0042	0.0198
NM_025498 // Psenen // presenilin enhancer 2 homolog (C. elegans)	Psenen/ Pen2	0.6368	**1.0088**	0.0002	0.0048
NM_021607 // Ncstn // nicastrin	Ncstn	0.0110	**-1.1471**	0.1094	0.0190
NM_007399 // Adam10 // disintegrin and metallopeptidase domain 10	Adam10	0.3788	**-1.0317**	0.0065	0.0163
NM_031156 // Ide // insulin degrading enzyme	Ide	0.0503	**1.0634**	0.0122	0.0090
NM_199307 // Ece1 // endothelin converting enzyme 1	Ece1	0.0513	**-1.1940**	0.1199	0.0756
NM_139293 // Ece2 // endothelin converting enzyme 2	Ece2	0.0674	**1.1258**	0.0559	0.0405
NM_008604 // Mme // membrane metallo endopeptidase / neprilysin	Mme/ NEP	0.7896	**1.0076**	0.0037	00114

Supplementary Table 5. mRNA expression changes of Aβ transporting & degrading enzymes and γ-secretase complex components in APP/PS1xABCC1$^{-/-}$ versus APP/PS1 mice (controls) reveals no differences.

Supplementary References

1. Craft, D.L., Wein, L.M., and Selkoe, D.J. 2002. A mathematical model of the impact of novel treatments on the A beta burden in the Alzheimer's brain, CSF and plasma. *Bull Math Biol* 64:1011-1031.
2. Kuhnke, D., Jedlitschky, G., Grube, M., Krohn, M., Jucker, M., Mosyagin, I., Cascorbi, I., Walker, L.C., Kroemer, H.K., Warzok, R.W., et al. 2007. MDR1-P-Glycoprotein (ABCB1) Mediates Transport of Alzheimer's amyloid-beta peptides--implications for the mechanisms of Abeta clearance at the blood-brain barrier. *Brain Pathol* 17:347-353.
3. Vogelgesang, S., Kunert-Keil, C., Cascorbi, I., Mosyagin, I., Schroder, E., Runge, U., Jedlitschky, G., Kroemer, H.K., Oertel, J., Gaab, M.R., et al. 2004. Expression of multidrug transporters in dysembryoplastic neuroepithelial tumors causing intractable epilepsy. *Clin Neuropathol* 23:223-231.
4. Lam, F.C., Liu, R., Lu, P., Shapiro, A.B., Renoir, J.M., Sharom, F.J., and Reiner, P.B. 2001. beta-Amyloid efflux mediated by p-glycoprotein. *J Neurochem* 76:1121-1128.
5. Vogelgesang, S., Cascorbi, I., Schroeder, E., Pahnke, J., Kroemer, H.K., Siegmund, W., Kunert-Keil, C., Walker, L.C., and Warzok, R.W. 2002. Deposition of Alzheimer's beta-amyloid is inversely correlated with P-glycoprotein expression in the brains of elderly non-demented humans. *Pharmacogenetics* 12:535-541.
6. Ahmed, M., Davis, J., Aucoin, D., Sato, T., Ahuja, S., Aimoto, S., Elliott, J.I., Van Nostrand, W.E., and Smith, S.O. 2010. Structural conversion of neurotoxic amyloid-beta(1-42) oligomers to fibrils. *Nat Struct Mol Biol* 17:561-567.
7. Bernstein, S.L., Dupuis, N.F., Lazo, N.D., Wyttenbach, T., Condron, M.M., Bitan, G., Teplow, D.B., Shea, J.-E., Ruotolo, B.T., Robinson, C.V., et al. 2009. Amyloid-b protein oligomerization and the importance of tetramers and dodecamers in the aetiology of Alzheimer's disease. *Nat Chemistry* 1:326-331.
8. Bernacki, J.P., and Murphy, R.M. 2009. Model discrimination and mechanistic interpretation of kinetic data in protein aggregation studies. *Biophys J* 96:2871-2887.
9. Walsh, D.M., and Selkoe, D.J. 2007. A beta oligomers - a decade of discovery. *J Neurochem* 101:1172-1184.
10. Vaz, A.I.F., and Vicente, L.N. 2007. A particle swarm pattern search method for bound constrained global optimization. *Journal of Global Optimization* 39:197-219.
11. Xue, W.F., Hellewell, A.L., Gosal, W.S., Homans, S.W., Hewitt, E.W., and Radford, S.E. 2009. Fibril fragmentation enhances amyloid cytotoxicity. *J Biol Chem* 284:34272-34282.
12. Daood, M., Tsai, C., Ahdab-Barmada, M., and Watchko, J.F. 2008. ABC transporter (P-gp/ABCB1, MRP1/ABCC1, BCRP/ABCG2) expression in the developing human CNS. *Neuropediatrics* 39:211-218.
13. Wesolowska, O., Molnar, J., Ocsovszki, I., and Michalak, K. 2009. Differential effect of phenothiazines on MRP1 and P-glycoprotein activity. In Vivo 23:943-947.